ARTICLE OPEN

Check for updates

Quadrupole topological insulators in $Ta_2M_3Te_5$ (M = Ni, Pd) monolayers

Zhaopeng Guo[1,2], Junze Deng[1,2], Yue Xie[1,2] and Zhijun Wang[1,2]✉

Higher-order topological insulators have been introduced in the precursory Benalcazar-Bernevig-Hughes quadrupole model, but no electronic compound has been proposed to be a quadrupole topological insulator (QTI) yet. In this work, we predict that $Ta_2M_3Te_5$ (M = Pd, Ni) monolayers can be 2D QTIs with second-order topology due to the double-band inversion. A time-reversal-invariant system with two mirror reflections (M_x and M_y) can be classified by Stiefel-Whitney numbers (w_1, w_2) due to the combined symmetry TC_{2z}. Using the Wilson loop method, we compute $w_1 = 0$ and $w_2 = 1$ for $Ta_2Ni_3Te_5$, indicating a QTI with $q^{xy} = e/2$. Thus, gapped edge states and localized corner states are obtained. By analyzing atomic band representations, we demonstrate that its unconventional nature with an essential band representation at an empty site, i.e., A_g@4e, is due to the remarkable double-band inversion on Y–Γ. Then, we construct an eight-band quadrupole model with M_x and M_y successfully for electronic materials. These transition-metal compounds of $A_2M_{1,3}X_5$ (A = Ta, Nb; M = Pd, Ni; X = Se, Te) family provide a good platform for realizing the QTI and exploring the interplay between topology and interactions.

npj Quantum Materials (2022)7:87 ; https://doi.org/10.1038/s41535-022-00498-8

INTRODUCTION

In higher-order topological insulators, the ingap states can be found in ($d-n$)-dimensional edges ($n > 1$), such as the corner states of two-dimensional (2D) systems or the hinge states of three-dimensional systems[1–12]. Different from topological insulators with ($d-1$)-dimensional edge states, the Chern numbers or $\mathbb{Z}_2$ numbers in higher-order topological insulators are zero. The higher-order topology can be captured by topological quantum chemistry[13–18], nested Wilson-loop method[1,8] and second Stiefel–Whitney (SW) class[19–25]. Using topological quantum chemistry[13], the higher-order topological insulator can be diagnosed by the decomposition of atomic band representations (aBRs) as an unconventional insulator (or obstructed atomic insulator) with mismatching of electronic charge centers and atomic positions[16–18,26]. In contrast to dipoles (Berry phase) for topological insulators, the higher-order topological insulators can be understood by multipole moments[1]. In a 2D system, the second-order topology corresponds to the quadrupole moment, which can be diagnosed by the nested Wilson-loop method[1,8,23]. When the system contains space-time inversion symmetries, such as PT and $C_{2z}T$, where the P and T represent inversion and time-reversal symmetries, the second-order topology can be described by the second SW number (w_2)[23,27]. The second SW number w_2 is a well-defined 2D topological invariant of an insulator only when the first SW number $w_1 = 0$. Usually, a 2D quadrupole topological insulator (QTI) with $w_1 = 0, w_2 = 1$ has gapped edge states and degenerate localized corner states, which are pinned at zero energy (being topological) in the presence of chiral symmetry. When the degenerate corner states are in the energy gap of bulk and edge states, the fractional corner charge can be maintained due to filling anomaly[28].

So far, various 2D systems are proposed to be SW insulators with second-order topology, such as monolayer graphdiyne[29,30], liganded Xenes[25,31], β-Sb monolayer[18] and Bi/EuO[32]. However, no compound has been proposed to be a QTI with M_x and M_y symmetries. After considering many-body interactions in transition-metal compounds, superconductivity, exciton condensation and Luttinger liquid could emerge in a transition-metal QTI. In recent years, van der Waals layered materials of $A_2M_{1,3}X_5$ (A = Ta, Nb; M = Pd, Ni; X = Se, Te) family have attracted attentions because of their special properties, such as quantum spin Hall effect in $Ta_2Pd_3Te_5$ monolayer[33,34], excitons in Ta_2NiSe_5[35–37], and superconductivity in $Nb_2Pd_3Te_5$ and doped $Ta_2Pd_3Te_5$[38]. In particular, the monolayers of $A_2M_{1,3}X_5$ family can be exfoliated easily, serving as a good platform for studying topology and interactions in lower dimensions.

In this work, we predict that based on first-principles calculations, $Ta_2Ni_3Te_5$ monolayer is a 2D QTI. Using the Wilson-loop method, we show that its SW numbers are $w_1 = 0$ and $w_2 = 1$, corresponding to the second-order topology. We also solve the aBR decomposition for $Ta_2Ni_3Te_5$ monolayer, and find that it is unconventional with an essential band representation (BR) at an empty Wykoff position (WKP), A_g@4c, which origins from the remarkable double-band inversion on Y–Γ line. To verify the QTI phase, we compute the energy spectrum of $Ta_2Ni_3Te_5$ monolayer with open boundary conditions in both x and y directions and obtain four degenerate corner states. Then, we construct an eight-band quadrupole model with M_x and M_y successfully. The double-band-inversion picture widely happens in the band structures of $A_2M_{1,3}X_5$ family. The $Ta_2M_3Te_5$ monolayers are 2D QTI candidates for experimental realization in electronic systems.

RESULTS

Band structures

The band structure of $Ta_2Ni_3Te_5$ monolayer suggests that it is an insulator with a band gap of 65 meV. We have checked that spin–orbit coupling (SOC) has little effect on the band structure (Supplementary Fig. 2b). We also checked the band structures using GW method and SCAN method, and we find that the band

[1]Beijing National Laboratory for Condensed Matter Physics, and Institute of Physics, Chinese Academy of Sciences, 100190 Beijing, China. [2]University of Chinese Academy of Sciences, 100049 Beijing, China. ✉email: wzj@iphy.ac.cn

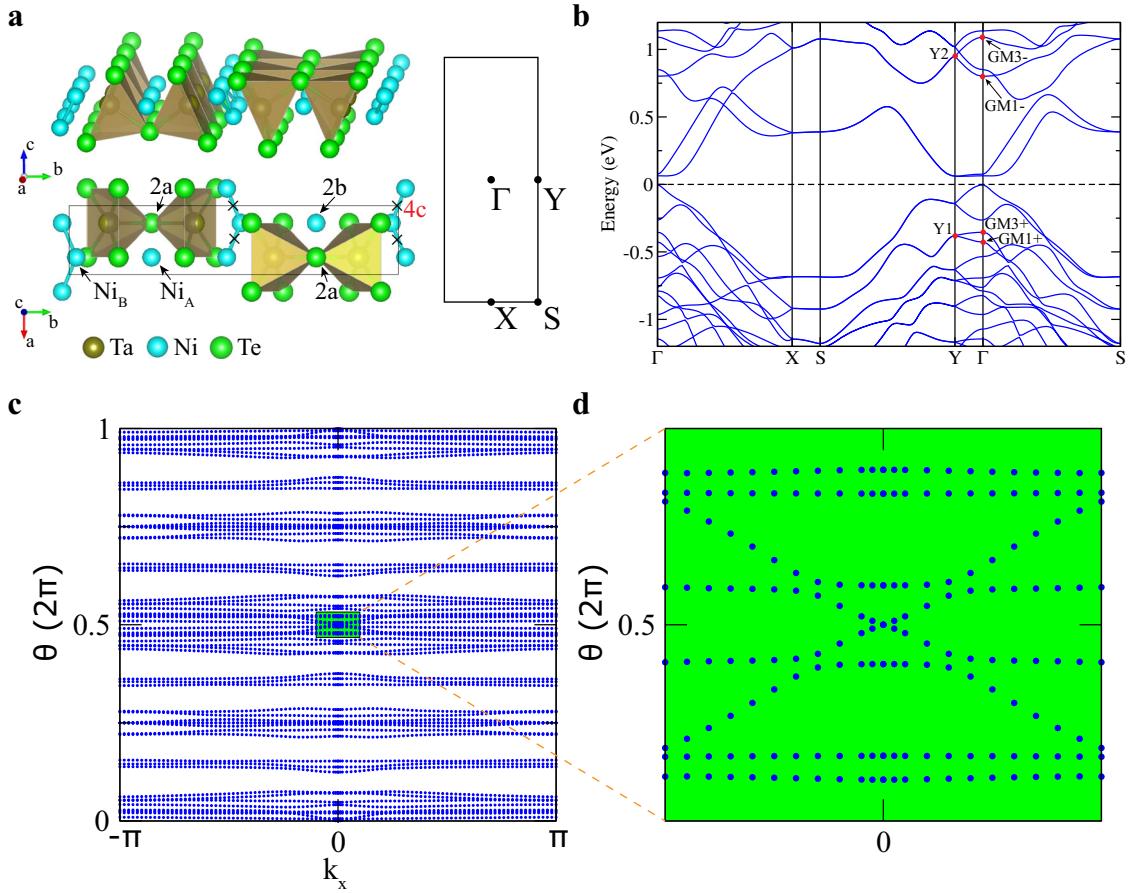

Fig. 1 Crystal structures and electronic structures of $Ta_2Ni_3Te_5$ monolayer. a The crystal structure, Wyckoff positions and Brillouin zone (BZ) of $Ta_2Ni_3Te_5$ monolayer. **b** Band structure and irreps at Y and Γ of $Ta_2Ni_3Te_5$ monolayer. **c** The 1D k_y-direct Wilson bands as a function of k_x calculated in the DFT code. **d** Close-up of the green region in (**c**), with one crossing of Wilson bands at $\theta = \pi$ indicating the second SW class $w_2 = 1$.

gap remains using these methods (the corresponding band structures are shown in Supplementary Note 1). As shown in the orbital-resolved band structures of Fig. 3a–c, although low-energy bands near the Fermi level (E_F) are mainly contributed by Ta-d_{z^2} orbitals (two conduction bands) and Ni_A-d_{xz} orbitals (two valence bands), the inverted bands of {Y2; GM1−, GM3−} come from Te-p_x orbitals. The irreducible representations (irreps)[39] at Y and Γ are denoted for the inverted bands in Fig. 1b. We notice that the double-band inversion between {Y2; GM1−, GM3−} bands and {Y1; GM1+, GM3+} bands is remarkable, about 1 eV.

Atomic band representations

To analyze the band topology, the decomposition of aBR is performed. In a unit cell of $Ta_2Ni_3Te_5$ monolayer in Fig. 1a, four Ta atoms, four Ni_B atoms and eight Te atoms are located at different 4*e* WKPs. The rest two Te atoms and two Ni_A atoms are located at 2*a* and 2*b* WKPs, respectively. The aBRs are obtained from the crystal structure by pos2aBR[16–18], and irreps of occupied states are calculated by IRVSP[39] at high-symmetry *k*-points. Then, the aBR decomposition is solved online—http://tm.iphy.ac.cn/UnconvMat.html. The results are listed in Supplementary Table 2 of Supplementary Note 2. Instead of being a sum of aBRs, we find that the aBR decomposition of the occupied bands has to include an essential BR at an empty WKP, i.e., A_g@4*c*. As illustrated in Fig. 1a, the charge centers of the essential BR are located at the middle of Ni_B-Ni_B bonds (i.e., the 4*c* WKP), indicating that the $Ta_2Ni_3Te_5$ monolayer is a 2D unconventional insulator with second-order topology.

Double-band inversion

In an ideal atomic limit, Te-*p* orbitals and Ni-*d* orbitals are occupied, while Ta-*d* orbitals are fully unoccupied. Thus, all the occupied bands are supposed to be the aBRs of Te-*p* and Ni-*d* orbitals, as shown in the left panel of Fig. 2a. However, in the monolayers of $A_2M_{1,3}X_5$ family (see their band structures in Supplementary Note 1), a double-band inversion happens between the occupied aBR A''@4*e* (Te-p_x and Ni-*d*) and unoccupied aBR A'@4*e* (Ta-d_{z^2}), as shown in the right two panels of Fig. 2a. When the double-band inversion happens between {Y2; GM1−, GM3−} and {Y1; GM2−, GM4−} on Y–Γ line, it results in a semimetal for Ta_2NiSe_5 monolayer (215-type; Fig. 2b). When it happens between {Y2; GM1−, GM3−} and {Y1; GM1+, GM3+} in Fig. 2c, the system becomes a 2D QTI for $Ta_2Ni_3Te_5$ monolayer (235-type), resulting in the essential BR of A_g@4*c*.

Second Stiefel–Whitney class $w_2 = 1$

To identify the second-order topology of the monolayers, we compute the second SW number by the Wilson-loop method. The first SW class (w_1) is

$$w_1|_C = \frac{1}{\pi}\oint_C \mathrm{d}\boldsymbol{k}\cdot \mathrm{Tr}\mathcal{A}(\boldsymbol{k}) \quad (1)$$

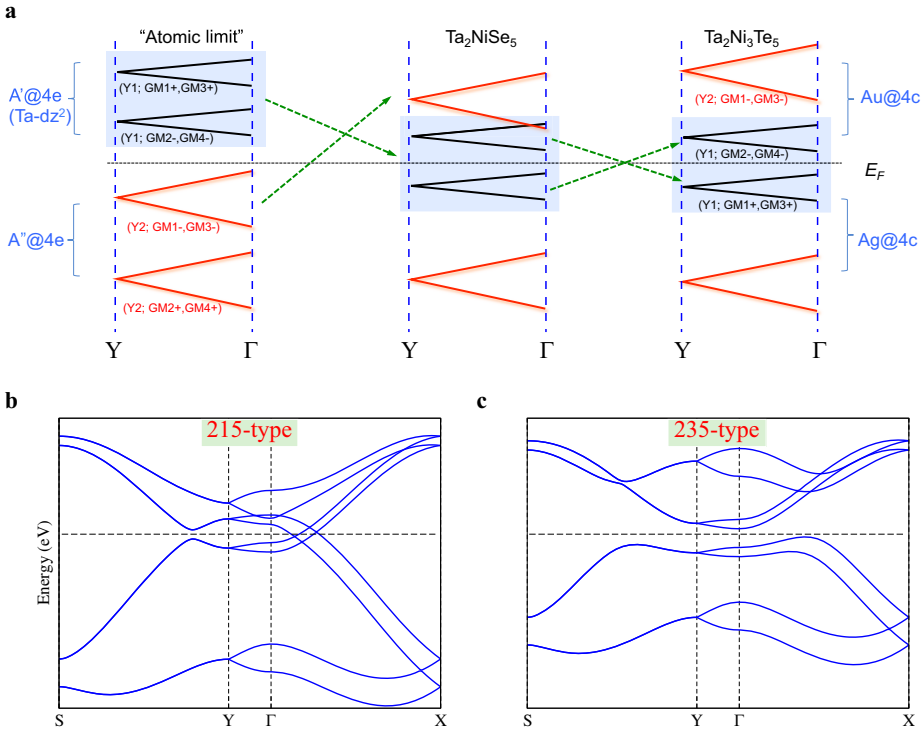

Fig. 2 The double-band inversion process. a The diagram of double-band inversion along Y–Γ line. The schematic band structures of (**b**) 215-type semimetal and (**c**) 235-type insulator. The double-band inversion happens in both cases. The crossing points on the Γ–X line are part of the nodal line.

where $\mathcal{A}_{mn}(\boldsymbol{k}) = \langle u_m(\boldsymbol{k})|i\nabla_{\boldsymbol{k}}|u_n(\boldsymbol{k})\rangle$[22]. The second SW class (w_2) can be computed by the nested Wilson-loop method, or simply by m module 2, where m is the number of crossings of Wilson bands at $\theta = \pi$. It should be noted that w_2 is well-defined only when $w_1 = 0$. With $w_1 = 0$, w_2 can be unchanged when choosing the unit cell shifting a half lattice constant. The 1D Wilson-loops are computed along k_y. The computed phases of the eigenvalues of Wilson-loop matrices $W_y(k_x)$ (Wilson bands) are shown in Fig. 1c as a function of k_x. The results show that the first SW class is $w_1 = 0$. In addition, there is one crossing of Wilson bands at $\theta = \pi$ [Fig. 1d], indicating the second SW class $w_2 = 1$. The quadruple moment $q^{xy} = e/2$ calculated by the nested Wilson-loop method in Supplementary Note 3. Therefore, the $Ta_2Ni_3Te_5$ monolayer is a QTI with a nontrivial second SW number.

Edge spectrum and corner states

From the orbital-resolved band structures (Fig. 3), the maximally localized Wannier functions of Ta-d_{z^2}, Ni$_A$-d_{xz} and Te-p_x orbitals are extracted, to construct a 2D tight-binding (TB) model of $Ta_2Ni_3Te_5$ monolayer. As shown in Fig. 3d, the obtained TB model fits the density functional theory (DFT) band structure well. First, we compute the (01)-edge spectrum with open boundary condition along y. Instead of gapless edge states for a 2D $\mathbb{Z}_2$-nontrivial insulator, gapped edge states are obtained for the 2D QTI [Fig. 3e]. Then, we explore corner states as the hallmark of the 2D QTI. We compute the energy spectrum for a nanodisk. For concreteness, we take a rectangular-shaped nanodisk with 50×10 unit cells, preserving both M_x and M_y symmetries in the 0D geometry. The obtained discrete spectrum for this nanodisk is plotted in the inset of Fig. 3f. Remarkably, one observes four degenerate states near E_F. The spatial distribution of these four-fold modes can be visualized from their charge distribution, as shown in Fig. 3f. Clearly, they are well localized at the four corners, corresponding to isolated corner states.

Minimum model for the 2D QTI

As shown in Fig. 2, the minimum model for the 2D QTI should be consisted of two BRs of A'@4e and A''@4e. Based on the situation of $Ta_2Ni_3Te_5$ monolayer in Fig. 2c, the minimum effective model is derived as below:

$$H_{\mathrm{TB}}(\boldsymbol{k}) = \begin{pmatrix} H_{\mathrm{Ta}}(\boldsymbol{k}) & H_{\mathrm{hyb}}(\boldsymbol{k}) \\ H_{\mathrm{hyb}}(\boldsymbol{k})^{\dagger} & H_{\mathrm{Ni}}(\boldsymbol{k}) \end{pmatrix} \tag{2}$$

The terms of $H_{\mathrm{Ta}}(\boldsymbol{k})$, $H_{\mathrm{Ni}}(\boldsymbol{k})$ and $H_{\mathrm{int}}(\boldsymbol{k})$ are 4×4 matrices, which read

$$\begin{aligned} H_{\mathrm{Ta}}(\boldsymbol{k}) &= [\varepsilon_s + 2t_{s1}\cos(k_x)]\sigma_0\tau_0 + t_{s2}\gamma_1(\boldsymbol{k}) + t_{s3}\sigma_0\tau_x, \\ H_{\mathrm{Ni}}(\boldsymbol{k}) &= [\varepsilon_p + 2t_{p1}\cos(k_x)]\sigma_0\tau_0 + t_{p2}\gamma_2(\boldsymbol{k}) + t_{p3}\sigma_0\tau_x, \\ H_{\mathrm{hyb}}(\boldsymbol{k}) &= 2it_{sp}\sin(k_x)\gamma_3(\boldsymbol{k}). \end{aligned} \tag{3}$$

The $\gamma_{1,2,3}(\boldsymbol{k})$ matrices are given explicitly in Supplementary Note 4.

We find that $t_{s1} < 0$ and $t_{p1}, t_{p2} > 0$ for the $A_2M_{1,3}X_5$ family (t_{s3} and t_{p3} are small). When $\varepsilon_s + 2t_{s1} - 2|t_{s2}| < \varepsilon_p + 2t_{p1} + 2t_{p2}$, the double-band inversion happens in the monolayers of this family. By fitting the DFT bands, we obtain $t_{s2} > 0$ for the 215-type, while $t_{s2} < 0$ for the 235-type. When $\varepsilon_p = -\varepsilon_s$ and $t_{pi} = -t_{si} (i = 1, 2, 3)$, the model is chiral symmetric (i.e., $\delta = 0$ in Table 1). Since the second SW insulator or QTI is topological in the presence of chiral symmetry, we would focus on the model (almost respecting chiral symmetry) in the following discussion.

Analytic solution of (01)-edge states

As the remnants of the QTI phase, the localized edge states can be solved analytically for the minimum model. For the (01)-edge, one

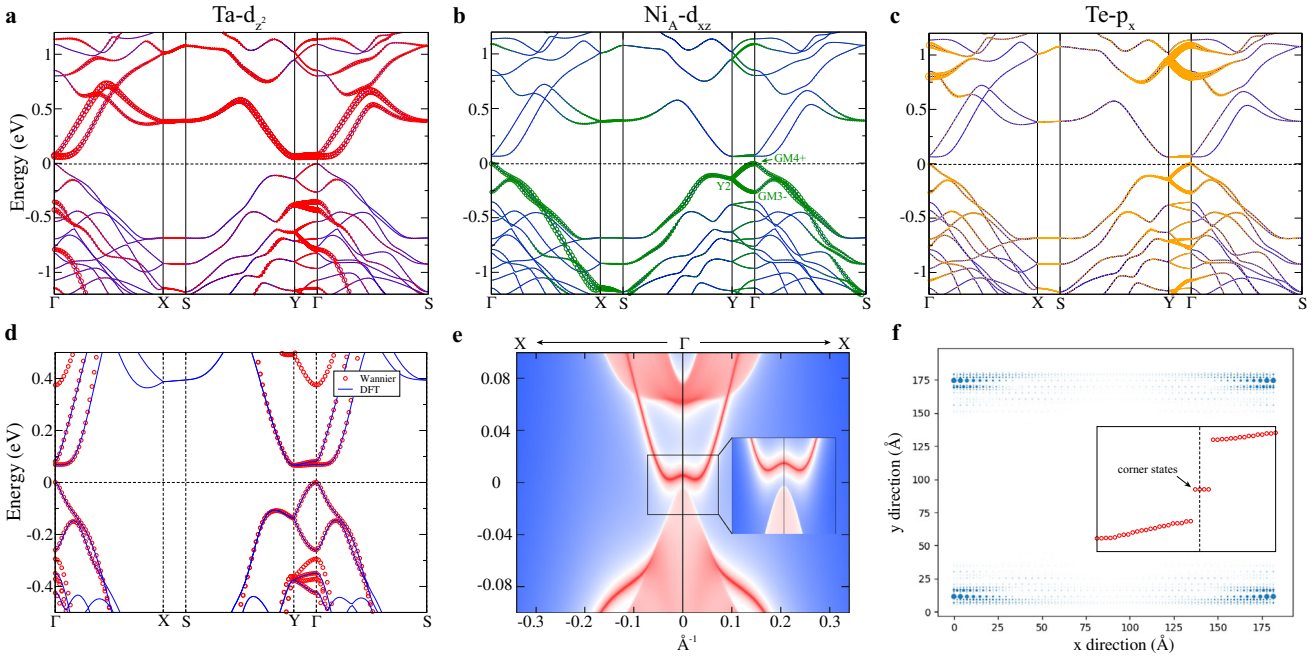

Fig. 3 The band structures and corner states of $Ta_2Ni_3Te_5$ monolayer. The orbital-resolved band structures of **a** d_{z^2} orbitals of Ta atoms, **b** d_{xz} orbitals of Ni_A atoms, and **c** p_x orbitals of Te atoms. **d** The comparison between band structures of maximally localized Wannier functions and DFT results. **e** (01)-edge states around Γ. **f** The charge distribution of four corner states. The insert shows the energy spectrum of the tight-binding model with open boundaries in x and y directions.

Table 1. Parameters of the TB model for the QTI with chiral symmetry when $\delta = 0$.

ε_s	t_{s1}	t_{s2}	t_{s3}	t_{sp}	ε_p	t_{p1}	t_{p2}	t_{p3}
2.05	−1	−0.8	−0.2	0.3	−2.05	1	0.8	0.2(1+δ)

can treat the model $H_{\rm TB}(\boldsymbol{k})$ as two parts, $H_0(\boldsymbol{k})$ and $H'(\boldsymbol{k})$,

$$\begin{aligned} H_0(\boldsymbol{k}) &= \begin{pmatrix} t_{s2}\gamma_1(\boldsymbol{k}) + t_{s3}\sigma_0\tau_x & 0 \\ 0 & t_{p2}\gamma_2(\boldsymbol{k}) + t_{p3}\sigma_0\tau_x \end{pmatrix} \\ H'(\boldsymbol{k}) &= \begin{pmatrix} [\varepsilon_s + 2t_{s1}\cos(k_x)]\sigma_0\tau_0 & H_{\rm hyb}(\boldsymbol{k}) \\ H_{\rm hyb}(\boldsymbol{k})^\dagger & [\varepsilon_p + 2t_{p1}\cos(k_x)]\sigma_0\tau_0 \end{pmatrix} \end{aligned} \tag{4}$$

Note that there is a pair of Dirac points $(\pm k_x^D, 0)$, with $k_x^D = \arccos\left[\frac{1}{2}\left(\frac{t_{s3}}{t_{s2}}\right)^2 - 1\right]$. Since k_x is still a good quantum number on the (01)-edge, expanding k_y to the second order, the zero-mode equation $H_0(k_x, -i\partial_y)\Psi(k_x, y) = 0$ can be solved for $y \in [0, +\infty)$. Taking the trial solution of $\Psi(k_x, y) = \psi(k_x)e^{\lambda y}$, we obtain the secular equation and the solution of $\lambda = \pm\lambda_\pm$, where

$$\lambda_\pm = 1 \pm \sqrt{\frac{t_{s3}^2}{(1+\cos(k_x))t_{s2}^2} - 1} \tag{5}$$

With the boundary conditions $\Psi(k_x, 0) = \Psi(k_x, +\infty) = 0$, only $-\lambda_\pm$ are permitted.

In the k_x regime of $\left[-\boldsymbol{k}_x^D, \boldsymbol{k}_x^D\right]$, the edge zero-mode states are $\Psi(k_x, y) = [C_1(k_x)\phi_1(k_x) + C_2(k_x)\phi_2(k_x)](e^{-\lambda_+ y} - e^{-\lambda_- y})$ with

$$\begin{aligned} \phi_1(k_x) &= \left(-\tfrac{(1+e^{-ik_x})t_{s2}}{t_{s3}} \quad 0 \quad 1 \quad 0 \quad 0 \quad 0 \quad 0 \quad 0\right)^{\rm T} \\ \phi_2(k_x) &= \left(0 \quad 0 \quad 0 \quad 0 \quad -\tfrac{t_{p3}}{(1+e^{ik_x})t_{p2}} \quad 0 \quad 1 \quad 0\right)^{\rm T} \end{aligned} \tag{6}$$

The edge zero states are Fermi arcs that linking the pair of projected Dirac points $(\pm k_x^D, 0)$. Once $H'(\boldsymbol{k})$ included, the effective (01)-edge Hamiltonian is,

$$\begin{aligned} H_{01}^{\rm eff} &= \langle\Phi|H(\boldsymbol{k})|\Phi\rangle \\ &= \begin{pmatrix} \varepsilon_s + 2t_{s1}\cos(k_x) & 0 \\ 0 & \varepsilon_p + 2t_{p1}\cos(k_x) \end{pmatrix} \end{aligned} \tag{7}$$

where $|\Phi\rangle \equiv |\phi_1(k_x), \phi_2(k_x)\rangle$. Two edge spectra are obtained in Fig. 4a.

Effective Su–Schrieffer–Heeger model on (10)-edge and corner states

Similarly, we derive the (10)-edge modes as $[F_1(k_y)\varphi_1(k_y) + F_2(k_y)\varphi_2(k_y)](e^{-\Lambda_+ x} - e^{-\Lambda_- x})$ with

$$\varphi_1 = \begin{pmatrix} 0 \\ 1-\Delta_s \\ 1-\Delta_s e^{ik_y} \\ 0 \\ -1+\Delta_p \\ 0 \\ 0 \\ -1+\Delta_p e^{-ik_y} \end{pmatrix}, \varphi_2 = \begin{pmatrix} e^{-ik_y}(1-\Delta_s) \\ 0 \\ 0 \\ 1-\Delta_s e^{-ik_y} \\ 0 \\ -1+\Delta_p \\ -e^{-ik_y}+\Delta_p \\ 0 \end{pmatrix}. \tag{8}$$

Here, $\Lambda_\pm = \frac{2t_{sp} \pm \sqrt{4t_{sp}^2 - 2(2t_{s1}+t_{s2})(2t_{s1}+2t_{s2}+\varepsilon_s)}}{2t_{s1}+t_{s2}}$, $\Delta_s = \left(\frac{t_{s3}}{2t_{s2}}\right)^2$, and $\Delta_p = \left(\frac{t_{p3}}{2t_{p2}}\right)^2$. Then we obtain the effective Hamiltonian on (10) edge below,

$$\begin{aligned} H_{10}^{\rm eff} &= \begin{pmatrix} 0 & v + we^{-ik_y} \\ v + we^{ik_y} & 0 \end{pmatrix}, \\ w &= t_{s3} + t_{p3} - 4t_{s3}\Delta_s, \\ v &= t_{s3} + t_{p3} - 4t_{p3}\Delta_p \end{aligned} \tag{9}$$

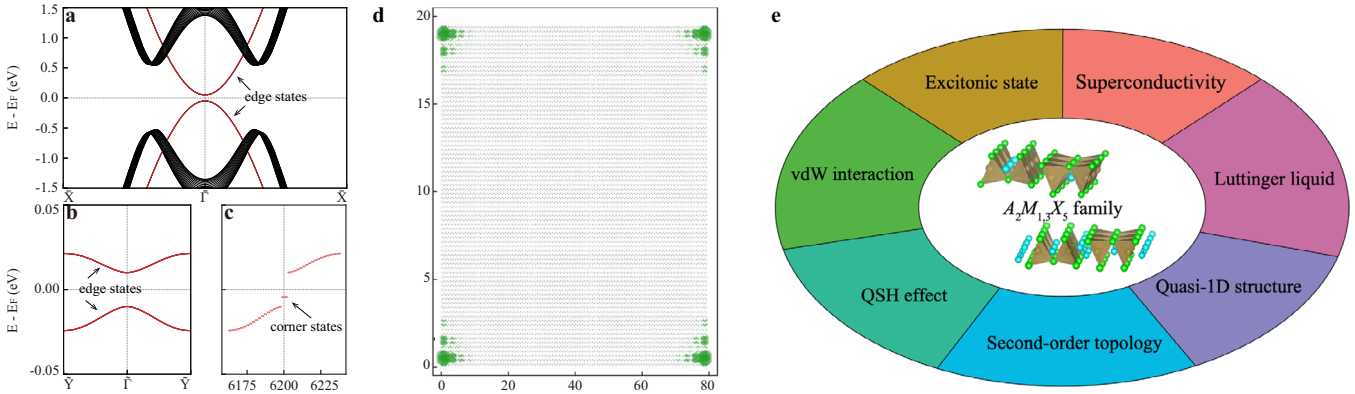

Fig. 4 The corner states of minimum model. Energy spectrum for **a** the (01)-edge, **b** the (10)-edge, and **c** a M_x- and M_y-symmetric disk of 80×20 unit cells of the minimum model with chiral symmetry slightly broken ($\delta = -0.1$). **d** The spatial distribution of four degenerate in-gap states in **c**. **e** The diverse properties of $A_2M_{1,3}X_5$ (A = Ta, Nb; M = Pd, Ni; X = Se, Te) family.

When $\delta = 0$, the minimum QTI model is chiral symmetric and it is gapless on the (10) edge (preserving M_y symmetry). When the chiral symmetry is slightly broken ($\delta \neq 0$), the H_{10}^{eff} becomes an Su–Schrieffer–Heeger model ($\delta < 0$ nontrivial; $\delta > 0$ trivial), as presented in Fig. 4b–d. As a result, we obtain a solution state on the end of the edge mode, i.e., the corner. As long as the energy of the corner state is located in the gap of bulk and edge states, the corner state is well localized at the corners, as shown in Fig. 4c, d.

DISCUSSION

In Ta_2NiSe_5 monolayer, the double-band inversion has also happened between Ta-d_{z^2} and Te-p_x states, about 0.4 eV, resulting in a semimetal with a pair of nodal lines in the 215-type. The highest valence bands on Y–Γ are from the inverted Ta-d_{z^2} states. However, in $Ta_2Ni_3Te_5$ monolayer, the double-band inversion strength becomes remarkable, ~1 eV, which is ascribed to the filled *B*-type voids and more extended Te-*p* states. On the other hand, the highest valence bands become Ni_A-d_{xz} states (slightly hybridized with Te-p_x states). It is insulating with a small gap of 65 meV. When it comes to $A_2Pd_3Te_5$ monolayer, the remarkable inversion strength is similar to that of $Ta_2Ni_3Te_5$. But the Pd_A-d_{xz} states go upwards further due to more expansion of the *d* orbitals and the energy gap becomes almost zero in $Ta_2Pd_3Te_5$. In short, the double-band inversion happens in all these monolayers, while the band gap of the 235-type changes from positive ($Ta_2Ni_3Te_5$), to nearly zero ($Ta_2Pd_3Te_5$ with a tiny band overlap), to negative ($Nb_2Pd_3Te_5$), as shown in Supplementary Fig. 1. Although the band structure of $Ta_2Pd_3Te_5$ bulk is metallic without SOC[33,34,38], the monolayer could become a QSH insulator upon including SOC in ref. [33]. Since their bulk materials are van der Waals layered compounds, the bulk topology and properties strongly rely on the band structures of the monolayers in the $A_2M_{1,3}X_5$ family.

As we find in ref. [33], the band topology of $Ta_2Pd_3Te_5$ monolayer is lattice sensitive. By applying >1% uniaxial compressive strain along *b*, it becomes a $\mathbb{Z}_2$-trivial insulator, being a QTI. On the other hand, due to the quasi-1D crystal structure, the screening effect of carriers is relatively weak and the electron-hole Coulomb interaction may be substantial for exciton condensation. The 1D in-gap edge states as remnants of the QTI are responsible for the observed Luttinger-liquid behavior.

In conclusion, we predict that $Ta_2M_3Te_5$ monolayers can be QTIs by solving aBR decomposition and computing SW numbers. Through aBR analysis, we conclude that the second-order topology comes from an essential BR at the empty site (A_g@4*c*), and it origins from the remarkable double-band inversion. The double-band inversion also happens in the band structure of Ta_2NiSe_5 monolayer. The second SW number of $Ta_2Ni_3Te_5$ monolayer is $w_2 = 1$, corresponding to a QTI. Therefore, we obtain edge states and corner states of the monolayer. The eight-band quadrupole model with M_x and M_y has been constructed successfully for electronic materials. With the large double-band inversion and small band energy gap/overlap, these transition-metal materials of $A_2M_{1,3}X_5$ family provide a good platform to study the interplay between the topology and interactions (Fig. 4e).

METHODS

Calculation method

Our first-principles calculations were performed within the framework of the DFT using the projector augmented wave method[40,41], as implemented in Vienna ab-initio simulation package (VASP)[42,43]. The Perdew–Burke–Ernzerhof (PBE) generalized gradient approximation exchange-correlations functional[44] was used. SOC was neglected in the calculations except in Supplementary Fig. 2b. We also used SCAN[45] and GW[46] method when checking the band gap. In the self-consistent process, $16 \times 4 \times 1$ *k*-point sampling grids were used, and the cut-off energy for plane wave expansion was 500 eV. The irreps were obtained by the program IRVSP[39]. The maximally localized Wannier functions were constructed by using the Wannier90 package[47]. The edge spectra are calculated using surface Green's function of semi-infinite system[48,49].

DATA AVAILABILITY

The data sets that support the findings in this study are available from the corresponding author upon request.

CODE AVAILABILITY

The codes that support the findings in this study are available from the corresponding author upon request.

Received: 8 June 2022; Accepted: 18 August 2022;
Published online: 03 September 2022

REFERENCES

1. Benalcazar, W. A., Bernevig, B. A. & Hughes, T. L. Quantized electric multipole insulators. *Science* **357**, 61–66 (2017).
2. Schindler, F. et al. Higher-order topological insulators. *Sci. Adv.* **4**, eaat0346 (2018).
3. Song, Z., Fang, Z. & Fang, C. (d-2)-dimensional edge states of rotation symmetry protected topological states. *Phys. Rev. Lett.* **119**, 246402 (2017).
4. Langbehn, J., Peng, Y., Trifunovic, L., von Oppen, F. & Brouwer, P. W. Reflection-symmetric second-order topological insulators and superconductors. *Phys. Rev. Lett.* **119**, 246401 (2017).
5. Schindler, F. et al. Higher-order topology in bismuth. *Nat. Phys.* **14**, 918–924 (2018).

6. Ezawa, M. Higher-order topological insulators and semimetals on the breathing kagome and pyrochlore lattices. *Phys. Rev. Lett.* **120**, 026801 (2018).
7. Khalaf, E. Higher-order topological insulators and superconductors protected by inversion symmetry. *Phys. Rev. B* **97**, 205136 (2018).
8. Wang, Z., Wieder, B. J., Li, J., Yan, B. & Bernevig, B. A. Higher-order topology, monopole nodal lines, and the origin of large Fermi arcs in transition metal dichalcogenides XTe_2 (X = Mo,W). *Phys. Rev. Lett.* **123**, 186401 (2019).
9. Benalcazar, W. A., Li, T. & Hughes, T. L. Quantization of fractional corner charge in C_n-symmetric higher-order topological crystalline insulators. *Phys. Rev. B* **99**, 245151 (2019).
10. Yue, C. et al. Symmetry-enforced chiral hinge states and surface quantum anomalous Hall effect in the magnetic axion insulator $Bi_{2-x}Sm_xSe_3$. *Nat. Phys.* **15**, 577–581 (2019).
11. Xu, Y., Song, Z., Wang, Z., Weng, H. & Dai, X. Higher-order topology of the axion insulator $EuIn_2As_2$. *Phys. Rev. Lett.* **122**, 256402 (2019).
12. Wieder, B. J. et al. Strong and fragile topological Dirac semimetals with higher-order Fermi arcs. *Nat. Commun.* **11**, 627 (2020).
13. Bradlyn, B. et al. Topological quantum chemistry. *Nature* **547**, 298–305 (2017).
14. Elcoro, L. et al. Magnetic topological quantum chemistry. *Nat. Commun.* **12**, 5965 (2021).
15. Gao, J., Guo, Z., Weng, H. & Wang, Z. Magnetic band representations, Fu-Kane-like symmetry indicators, and magnetic topological materials. *Phys. Rev. B* **106**, 035150 (2022).
16. Nie, S. et al. Application of topological quantum chemistry in electrides. *Phys. Rev. B* **103**, 205133 (2021).
17. Nie, S., Bernevig, B. A. & Wang, Z. Sixfold excitations in electrides. *Phys. Rev. Res.* **3**, L012028 (2021).
18. Gao, J. et al. Unconventional materials: the mismatch between electronic charge centers and atomic positions. *Sci. Bull.* **67**, 598–608 (2022).
19. Fang, C., Chen, Y., Kee, H.-Y. & Fu, L. Topological nodal line semimetals with and without spin-orbital coupling. *Phys. Rev. B* **92**, 081201 (2015).
20. Zhao, Y. X., Schnyder, A. P. & Wang, Z. D. Unified theory of PT and CP invariant topological metals and nodal superconductors. *Phys. Rev. Lett.* **116**, 156402 (2016).
21. Zhao, Y. X. & Lu, Y. PT-symmetric real Dirac fermions and semimetals. *Phys. Rev. Lett.* **118**, 056401 (2017).
22. Ahn, J., Park, S., Kim, D., Kim, Y. & Yang, B.-J. Stiefel-Whitney classes and topological phases in band theory. *Chin. Phys. B* **28**, 117101 (2019).
23. Ahn, J., Park, S. & Yang, B.-J. Failure of Nielsen-Ninomiya theorem and fragile topology in two-dimensional systems with space-time inversion symmetry: Application to twisted bilayer graphene at magic angle. *Phys. Rev. X* **9**, 021013 (2019).
24. Wu, Q., Soluyanov, A. A. & Bzdusek, T. Non-abelian band topology in non-interacting metals. *Science* **365**, 1273–1277 (2019).
25. Pan, M., Li, D., Fan, J. & Huang, H. Two-dimensional Stiefel-Whitney insulators in liganded Xenes. *NPJ Comput. Mater.* **8**, 1–6 (2022).
26. Xu, Y. et al. Three-dimensional real space invariants, obstructed atomic insulators and a new principle for active catalytic sites. Preprint at http://arxiv.org/abs/2111.02433 (2021).
27. Wieder, B. J. & Bernevig, B. A. The axion insulator as a pump of fragile topology. Preprint at http://arxiv.org/abs/1810.02373 (2018).
28. Benalcazar, W. A., Li, T. & Hughes, T. L. Quantization of fractional corner charge in C_n-symmetric higher-order topological crystalline insulators. *Phys. Rev. B* **99**, 245151 (2019).
29. Sheng, X.-L. et al. Two-dimensional second-order topological insulator in graphdiyne. *Phys. Rev. Lett.* **123**, 256402 (2019).
30. Lee, E., Kim, R., Ahn, J. & Yang, B.-J. Two-dimensional higher-order topology in monolayer graphdiyne. *NPJ Quantum Mater.* **5**, 1–7 (2020).
31. Qian, S., Liu, C.-C. & Yao, Y. Second-order topological insulator state in hexagonal lattices and its abundant material candidates. *Phys. Rev. B* **104**, 245427 (2021).
32. Chen, C. et al. Universal approach to magnetic second-order topological insulator. *Phys. Rev. Lett.* **125**, 056402 (2020).
33. Guo, Z. et al. Quantum spin Hall effect in $Ta_2M_3Te_5$ (M = Pd, Ni). *Phys. Rev. B* **103**, 115145 (2021).
34. Wang, X. et al. Observation of topological edge states in the quantum spin Hall insulator $Ta_2Pd_3Te_5$. *Phys. Rev. B* **104**, L241408 (2021).
35. Wakisaka, Y. et al. Excitonic insulator state in Ta_2NiSe_5 probed by photoemission spectroscopy. *Phys. Rev. Lett.* **103**, 026402 (2009).
36. Lu, Y. F. et al. Zero-gap semiconductor to excitonic insulator transition in Ta_2NiSe_5. *Nat. Commun.* **8**, 14408 (2017).
37. Mazza, G. et al. Nature of symmetry breaking at the excitonic insulator transition: Ta_2NiSe_5. *Phys. Rev. Lett.* **124**, 197601 (2020).
38. Higashihara, N. et al. Superconductivity in $Nb_2Pd_3Te_5$ and chemically-doped $Ta_2Pd_3Te_5$. *J. Phys. Soc. Jpn.* **90**, 063705 (2021).
39. Gao, J. C., Wu, Q. S., Persson, C. & Wang, Z. J. Irvsp: to obtain irreducible representations of electronic states in the VASP. *Comp. Phys. Commun.* **261**, 107760 (2021).
40. Blochl, P. E. Projector augmented-wave method. *Phys. Rev. B* **50**, 17953 (1994).
41. Kresse, G. & Joubert, D. From ultrasoft pseudopotentials to the projector augmented-wave method. *Phys. Rev. B* **59**, 1758 (1999).
42. Kresse, G. & Furthmuller, J. Efficiency of ab-initio total energy calculations for metals and semiconductors using a plane-wave basis set. *Comp. Mater. Sci.* **6**, 15–50 (1996).
43. Kresse, G. & Furthmuller, J. Efficient iterative schemes for ab initio total-energy calculations using a plane-wave basis set. *Phys. Rev. B* **54**, 11169 (1996).
44. Perdew, J. P., Burke, K. & Ernzerhof, M. Generalized gradient approximation made simple. *Phys. Rev. Lett.* **77**, 3865 (1996).
45. Sun, J., Ruzsinszky, A. & Perdew, J. Strongly constrained and appropriately normed semilocal density functional. *Phys. Rev. Lett.* **115**, 036402 (2015).
46. Shishkin, M. & Kresse, G. Implementation and performance of the frequency-dependent GW method within the PAW framework. *Phys. Rev. B* **74**, 035101 (2006).
47. Pizzi, G. et al. Wannier90 as a community code: new features and applications. *J. Phys. Condens. Matter* **32**, 165902 (2020).
48. Sancho, M. P. L., Sancho, J. M. L. & Rubio, J. Quick iterative scheme for the calculation of transfer-matrices - application to Mo(100). *J. Phys. F: Met. Phys.* **14**, 1205–1215 (1984).
49. Sancho, M. P. L., Sancho, J. M. L. & Rubio, J. Highly convergent schemes for the calculation of bulk and surface Green-functions. *J. Phys. F: Met. Phys.* **15**, 851–858 (1985).

ACKNOWLEDGEMENTS

This work was supported by the National Natural Science Foundation of China (Grant Nos. 11974395 and 12188101), the Strategic Priority Research Program of Chinese Academy of Sciences (Grant No. XDB33000000), the China Postdoctoral Science Foundation funded project (Grant No. 2021M703461), and the Center for Materials Genome.

AUTHOR CONTRIBUTIONS

Z.W. conceived and supervised the work. Z.G. performed the first-principles calculation. J.D. and Y.X. contributed to the analytical modeling. All authors contributed to the discussion and wrote the manuscript.

COMPETING INTERESTS

The authors declare no competing interests.

ADDITIONAL INFORMATION

Supplementary information The online version contains supplementary material available at https://doi.org/10.1038/s41535-022-00498-8.

Correspondence and requests for materials should be addressed to Zhijun Wang.

Reprints and permission information is available at http://www.nature.com/reprints

Publisher's note Springer Nature remains neutral with regard to jurisdictional claims in published maps and institutional affiliations.